Journal of Materials Chemistry A

ROYAL SOCIETY OF CHEMISTRY

PAPER

View Article Online
View Journal | View Issue

Cite this: J. Mater. Chem. A, 2021, 9, 12782

Correlating MOF-808 parameters with mixed-matrix membrane (MMM) CO_2 permeation for a more rational MMM development†

Raymond Thür,[a] Daan Van Havere,[a] Niels Van Velthoven,[a] Simon Smolders,[a] Aran Lamaire,[b] Jelle Wieme,[b] Veronique Van Speybroeck,[b] Dirk De Vos[a] and Ivo F. J. Vankelecom *[a]

Consistent structure–performance relationships for the design of MOF (metal–organic framework)-based mixed-matrix membranes (MMMs) for gas separation are currently scarce in MMM literature. An important step in establishing such relationships could be to correlate intrinsic MOF parameters, such as CO_2 uptake and the CO_2 adsorption enthalpy (Q_{st}), with the separation performance indicators of the MMM (*i.e.* separation factor and permeability). Such a study presumes the availability of a platform MOF, which allows systematic comparison of the relevant MOF parameters. MOF-808 can take up the role of such a platform MOF, owing to its unique cluster coordination and subsequent ease of introducing additional functional molecules. For this purpose, formic acid (FA) modulated MOF-808 (MOF–FA) was post-synthetically functionalized with five different ligands (histidine (His), benzoic acid (BA), glycolic acid (GA), lithium sulfate (Li_2SO_4) and trifluoroacetic acid (TFA)) to create a series of isostructural MOFs with varying affinity/diffusivity properties but as constant as possible remaining properties (*e.g.* particles size distribution). CO_2 uptake and CO_2 adsorption enthalpy of the MOFs were determined with CO_2 sorption experiments and Clausius–Clapeyron analysis. These MOF properties were subsequently linked to the CO_2/N_2 separation factor and CO_2 permeability of the corresponding MMM. Unlike what is often assumed in literature, MOF-808 CO_2 uptake proved to be a poor indicator for MMM performance. In contrast, a strong correlation was observed between Q_{st} at high CO_2 loadings on one hand and CO_2 permeability under varying feed conditions on the other hand. Furthermore, correlation coefficients of $Q_{st,15}$ and $Q_{st,30}$ (Q_{st} at 15 and 30 cm^3 (STP) g^{-1}) with the separation factor were significantly better than those calculated for CO_2 uptake. The surprising lack of correlation between membrane performance and CO_2 uptake and the strong correlation with Q_{st} opens possibilities to rationally design MMMs and stresses the need for more fundamental research focused on finding consistent relationships between filler properties and the final membrane performance.

Received 19th October 2020
Accepted 11th May 2021

DOI: 10.1039/d0ta10207e

rsc.li/materials-a

1 Introduction

Mixed-matrix membranes (MMMs) consist of a continuous polymer matrix containing dispersed nanoparticles (so-called fillers).[1,2] While polymeric membranes show good processability but rather moderate gas separation performance,[3,4] purely inorganic membranes can reach high selectivity/permeance combinations due to their particular size sieving abilities or strong affinity for the target component.[5] However, inorganic membranes are often uneconomical to produce as they are brittle, making it challenging to prepare up-scaled membranes with large specific surface.[6] MMMs are believed to profit from the best of both worlds, having improved separation capacity due to nanoparticle addition while maintaining the good film-forming properties of the polymer. Much research has been dedicated in the past 10 years to find better combinations of polymers and MOFs with enhanced performance compared to the state-of-the-art.[2,7–13] A lot of these literature reports focus on the use and modification of conventional MOFs, frequently employing a trial-and-error approach for developing novel MMMs. Although the membrane performance can indeed often be boosted by incorporation of MOFs in terms of higher permeability or gas pair selectivity, the theoretical understanding behind the MMM concept remains rather poor and consistent structure–performance relationships for the

[a]Centre for Membrane Separations, Adsorption, Catalysis and Spectroscopy for Sustainable Solutions (cMACS), KU Leuven, Celestijnenlaan 200F, Box 2454, Heverlee, 3001, Belgium

[b]Center for Molecular Modeling, Ghent University, Tech Lane Ghent Science, Park Campus A, Technologiepark 46, Zwijnaarde, 9052, Belgium. E-mail: ivo.vankelecom@kuleuven.be; Tel: +32 16 32 15 94

† Electronic supplementary information (ESI) available. See DOI: 10.1039/d0ta10207e

design of MMMs are currently very scarce.[14,15] A first step towards finding such structure–performance relationships could be the linking of intrinsic MOF parameters to the gas permeation behavior of the MMM (thus determining indicators for the MMM separation performance based on MOF parameters). For example, Seoane and co-workers proposed a method to quantify polymer-MOF compatibility based on the Hansen solubility parameters of MOF and polymer.[1] With respect to the membrane selectivity and permeability, MOF parameters such as pore volume and CO_2 uptake are often identified as key drivers in the ultimate MMM performance, where good MMM separation performance goes hand in hand with high pore volume and CO_2 uptake.[16–21] However, no study has been devoted so far to the systematic correlation between MOF and MMM parameters for a series of isostructural MOFs. This is understandable since such a study presumes the availability of a platform MOF, which allows systematic comparison of the relevant MOF parameters. Furthermore, the overall gas permeation through the MMM is the result of a subtle interplay between polymer and MOF-related factors, which complicates the identification of one-on-one correlations and causalities between parameters.

MOF-808, consisting of the same $Zr_6O_4(OH)_4$ cluster as UiO-66 but linked through six 1,3,5-benzenetricarboxylate (BTC^{3-}) linkers, can take up the role of such a platform MOF since it can be simply modified to change intrinsic MOF properties while preserving the same MOF structure and topology.[10] Next to the six BTC^{3-} linkers occupying the binding sites (at opposing vertices of the cluster), the six equatorial binding sites can theoretically be occupied by up to six modulator or ligand molecules[22] (Fig. 1), which can be easily attached *via* solvent-assisted ligand exchange.[23] As shown in previous work, it is possible to create isostructural MOF-808 derivatives with subtly altered BET surface area, pore volume, CO_2 uptake and CO_2 affinity.[10] Moreover, other appealing features of MOF-808 include its excellent thermal, chemical and mechanical stability, following from the strong interaction of the Zr_6-cluster and the carboxylate ligands, and the easy up-scaling of the synthesis in non-toxic solvents such as water.[24]

In this work, post-synthetic functionalization of MOF-808 was applied to create a series of isostructural MOF-808 with systematically varying characteristics, such as pore volume, surface area, CO_2 uptake and CO_2 adsorption enthalpy (Q_{st}). For this purpose, a single batch of MOF–FA was produced to guarantee a uniform starting material for all functionalizations, hence avoiding differences in MOF morphology or particle size due to batch variations. Five different functional molecules (histidine (His), benzoic acid (BA), glycolic acid (GA), lithium sulfate (Li_2SO_4) and trifluoroacetic acid (TFA)) were selected based on their anticipated interaction with CO_2. The polyimide Matrimid 5218 (Matrimid) was used as polymer matrix as it is regarded as a benchmark polymer for membrane gas separation tests in academic research.[1,25–27] The obtained MOF characteristics were correlated with the MMM performance parameters (CO_2/N_2 separation factor, pure gas permeability (PGP) and mixed-gas permeability) in an attempt to identify the MOF

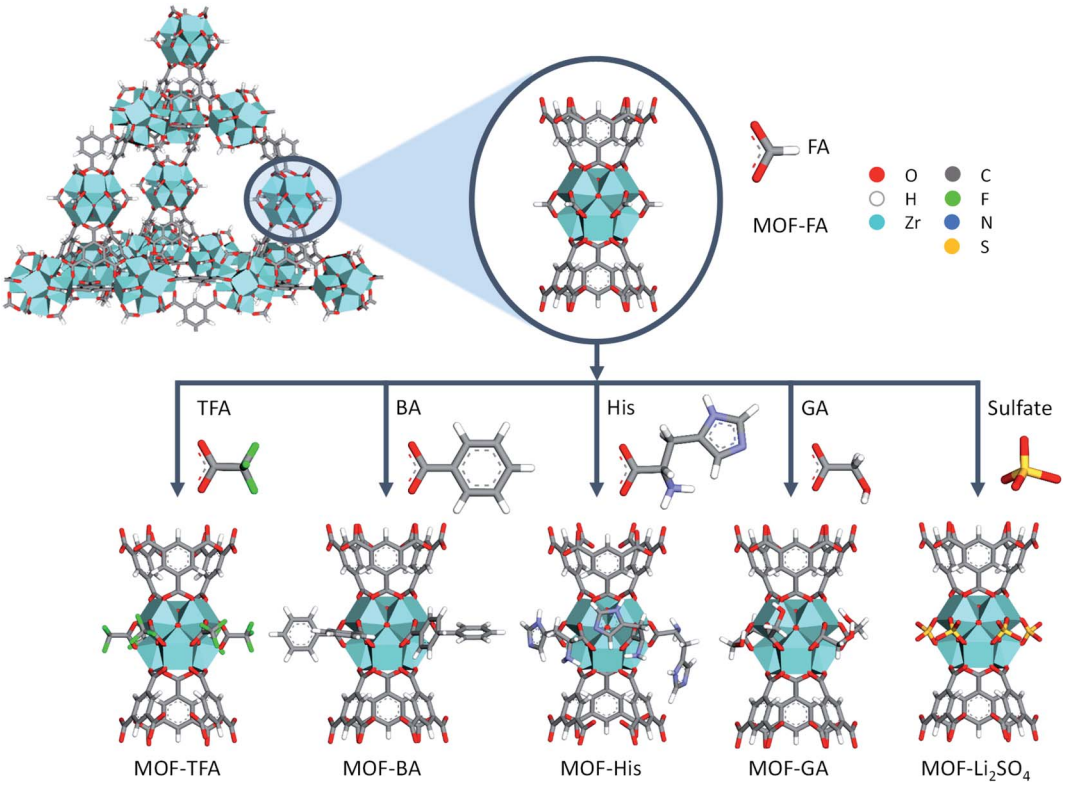

Fig. 1 Overview of MOF-808 functionalization strategy. FA = formic acid, TFA = trifluoroacetic acid, BA = benzoic acid, His = histidine, GA = glycolic acid. For clarity, lithium ions are not shown.

parameters that are best suited to use as predictors for the MMM permeation behavior.

2 Experimental and methodology section

2.1 Chemicals

Polyimide (Matrimid 5218) was kindly provided by Huntsman (Switzerland). Sulfuric acid (99.9%), $Li_2SO_4 \cdot H_2O$ (>98.5%), BA (>99.5%), GA (99%) and histidine (L, >99%) were purchased from Sigma-Aldrich. TFA (99%) was acquired from Merck-Schuchardt. FA (99%), tetrahydrofuran (THF, >99%), dimethylsulfoxide (DMSO, 99%) acetone (technical grade) and ethanol (pure) were supplied by Acros. Zirconylchloride octahydrate ($ZrOCl_2 \cdot 8H_2O$) was acquired from Abcr GmbH and BTC from J & K Chemicals. CO_2 (>99.999%) and N_2 (>99.999%) were purchased from Air Liquide and used as delivered.

2.2 MOF synthesis

The different MOF-808 samples are denoted as MOF-*x*, with *x* being the ligand type, *e.g.* MOF-808 functionalized with BA is denoted as MOF–BA. A single batch of MOF–FA was prepared (yield 12.6 g) to prevent differences between samples due to batch variations. All functionalized MOFs were synthesized using MOF–FA as starting material.

2.2.1 Synthesis of MOF–FA. The MOF synthesis recipe used in previous work[10] was adapted for using FA as modulator and subsequently scaled up. 5.08 g (24.2 mmol) BTC and 23.4 g (72.8 mmol) $ZrOCl_2 \cdot 8H_2O$ were dissolved in 182 mL H_2O in a 500 mL round-bottom flask. Subsequently, 26.8 mL FA (712 mmol) was added and the mixture was thoroughly stirred for 15 min. The reaction mixture was then heated to 100 °C under reflux for 5 h in an oil bath. The formed MOF sludge was transferred into Falcon tubes and washed with distilled water (30 mL). After 8 h, the MOF samples were centrifuged (4000 rpm, 30 min) and the supernatant was decanted. This was repeated 4 times with distilled water and 3 times with ethanol. After the last washing step, a clean, white powder (12.6 g) was obtained by drying in a vacuum oven at 70 °C overnight.

2.2.2 Synthesis of MOF–BA. MOF–BA was functionalized according to the method developed by Baek *et al.*[28] 250 mg of MOF–FA was suspended in a 50 mL DMSO solution with 1.12 g (9.251 mmol) BA in a 100 mL Schott bottle. The bottle was then placed in an oil bath at 100 °C under constant stirring. After 24 h, the reaction was stopped and the reaction mixture poured into Falcon tubes and washed with DMSO (3 times, 30 mL) and acetone (3 times, 30 mL), similar to the washing procedure of MOF–FA. After washing, the MOF was dried at 70 °C and stored for further use.

2.2.3 Synthesis of MOF–His, MOF–TFA and MOF–GA. MOF–FA (250 mg) was suspended in a 50 mL aqueous solution of 0.005 mol ligand (0.78 g histidine, 0.57 g TFA, 0.38 g GA) in a 100 mL Schott bottle. The bottle was placed on a stirring plate for 24 h at room temperature. Afterwards, the functionalized MOFs were washed 3 times with water and 3 times with acetone, similar to the washing procedure of MOF–FA. Finally, the MOFs were dried at 70 °C and stored for further use.

2.2.4 Synthesis of MOF–Li_2SO_4. An aqueous solution of sulfuric acid (0.1 M, 50 mL) was prepared in a 100 mL Schott bottle by mixing 0.268 mL sulfuric acid with 49.732 mL water, in which 250 mg of MOF–FA was suspended to form MOF–SO_4. The mixture was stirred for 24 h at room temperature. Next, MOF–SO_4 was washed with water and acetone, dried and re-suspended in a 50 mL aqueous solution containing 0.64 g (0.005 mol) $Li_2SO_4 \cdot H_2O$ for 24 h under continuous stirring. The resulting MOF was washed with water (3 times) and with acetone (3 times), dried at 70 °C and stored for further use.

2.3 Membrane synthesis

The different Matrimid MMMs are denoted as MMM-*x*, with *x* being the ligand type. For example, the Matrimid MMM containing MOF–TFA is denoted as MMM–TFA.

2.3.1 Preparation of pristine Matrimid membranes. Matrimid membranes were prepared by dissolving 0.42 g of polymer in 5.58 g THF. After stirring overnight, the polymer solution was poured into a Teflon Petri dish (d = 6 cm) in a nitrogen bag. Evaporation of the solvent was slowed down by placing a plastic funnel over the Petri dish. Once the membrane had solidified due to solvent evaporation, the polymer film was removed from the Petri dish and annealed in a muffle oven by heating from room temperature to 110 °C at 5 °C min^{-1}. The membrane remained at this temperature for 2 h. Next, the membrane was heated at 5 °C min^{-1} to 180 °C for 6 h. Subsequently, the membranes were allowed to cool down naturally.

2.3.2 Mixed-matrix membrane synthesis. 10 wt% MMMs were prepared by dispersing 0.047 g of dried MOF in 5.58 g THF. The dispersion was then thoroughly sonicated for 15 min. Following an adapted priming protocol,[20] 0.42 g polymer was added to the dispersion in three steps (0.14 g per turn). All samples were continuously stirred on a magnetic stirring plate. Before and after polymer addition, the samples were sonicated for 15 min. After the final polymer addition, the polymer/MOF dispersion was stirred overnight and cast into a Petri dish (d = 6 cm) in a nitrogen bag. Evaporation of the solvent was slowed down by placing a plastic funnel over the Petri dish. Once the membrane had solidified due to solvent evaporation, the polymer film was removed from the Petri dish and annealed in a muffle oven by heating from room temperature to 110 °C at 5 °C min^{-1}. The membrane remained at this temperature for 2 h. Next, the membrane was heated at 5 °C min^{-1} to 180 °C for 6 h. The membranes were finally allowed to cool down naturally. Filler loading was determined with the following equation:

$$\text{Filler loading (wt\%)} = 100 \times \left(\frac{m_{\text{filler}}}{m_{\text{filler}} + m_{\text{polymer}}} \right) \quad (1)$$

with m_{filler} and m_{polymer} the weight of the filler and polymer, respectively.

2.4 Characterization

2.4.1 X-ray diffraction. MOF crystallinity was analyzed with X-ray diffraction (XRD). XRD diffractograms were measured by

a Malvern PANanlytical Empyrean diffractometer in transmission mode over a 1.3–45° 2θ range. A PIXcel3D solid-state detector and Cu anode (Cu Kα1: 1.5406 Å; Cu Kα2: 1.5444 Å) were used for detection and X-ray generation.

2.4.2 Nuclear magnetic resonance. Proton and fluorine nuclear magnetic resonance (^{1}H and ^{19}F NMR) measurements were carried out to determine the average number of functionalizer molecules per Zr_6 cluster. First, 3 mg MOF-808 was dispersed in 600 μL deuterated DMSO. Next, 25 μL of a 40 wt% hydrofluoric acid (HF) solution was added for MOF digestion. For ^{19}F NMR, 10 μL fluorobenzene was added to the mixture as an internal standard. NMR spectra were recorded on a Bruker AMX-300 spectrometer at 300 MHz for ^{1}H NMR and at 400 MHz for ^{19}F NMR (16 scans). A recycle delay time of 30 s was applied for ^{19}F NMR. The output was analyzed with SpinWorks 4.2 software.

2.4.3 Scanning electron microscopy. Particle morphology was examined with scanning electron microscopy (SEM, Philips XL30 FEG). To avoid sample charging, all samples were coated with a layer of gold/palladium. Particle size distribution was analyzed with ImageJ and statistical analysis (one-way ANOVA) to determine whether differences in size occurred between the MOFs.

2.4.4 Attenuated total reflectance-Fourier transform infrared spectroscopy. Attenuated total reflectance-Fourier transform infrared spectroscopy (ATR-FTIR) measurements on MOF and MMM samples were conducted to identify functional groups. All samples were dried prior to the measurement. A Varian 670 FTIR imaging spectrometer was used, containing a diamond ATR crystal and a Single Point MCT detector. 32 scans were recorded at a resolution of 2 cm^{-1}.

2.4.5 N_2 and CO_2 physisorption. N_2 and CO_2 physisorption experiments were performed with a Micromeritics 3Flex surface analyzer. Prior to the measurement, all MOFs were activated under vacuum at 100 °C for 16 h. N_2 physisorption was conducted at −196 °C. Surface areas were calculated *via* the multipoint BET method applied to the isotherm adsorption branch, taking into account surface area criteria as given by Rouquerol[29] and the consistency criteria described by Walton and Snurr.[30] CO_2 sorption was measured at three different temperatures (273 K, 293 K, 313 K) to allow determination of the CO_2 Q_{st} of the different MOFs with the Clausius–Clapeyron equation (eqn (2)):[31]

$$\frac{\partial \ln(p)}{\partial\left(\frac{1}{T}\right)} = \frac{-Q_{st}}{R} \tag{2}$$

with p the equilibrium pressure (mbar), T the temperature (K), R the universal gas constant (J mol^{-1} K^{-1}).

The sorption data were first fitted with the dual-site Langmuir model (eqn (3)):[31]

$$N = N_{m,A} \times \frac{b_A \times p}{1 + b_A \times p} + N_{m,B} \times \frac{b_B \times p}{1 + b_B \times p} \tag{3}$$

with N the amount of adsorbed gas (cm^3 (STP) g^{-1}), $N_{m,A}$ and $N_{m,B}$ the amount of adsorbed gas at saturation for sorption site A and B respectively (cm^3 (STP) g^{-1}), b_A and b_B the adsorption equilibrium constants for respectively sorption site A and B and p the pressure (mbar).

The Clausius–Clapeyron data points were then interpolated based on the fit values. Next, for a range of different CO_2 loadings, Q_{st} can be calculated from the slope of a $\ln(p)$ *vs.* $1/T$ plot, according to eqn (2).

2.4.6 Membrane gas sorption. Sorption of N_2 and CO_2 was measured at 30 °C up to pressures of 15 bar for all membranes. A Rubotherm series IsoSORP© instrument was used to conduct the measurements. First, helium pycnometry was carried out on all membranes to determine the membrane weight and volume. The additional weight resulting from gas sorption in the membrane over time was determined with a magnetically suspended balance. The buoyancy of the measurement gases was taken into account to calculate the correct weight of the sample (eqn (4)):

$$m_{corrected} = m_{measured} + \rho_{gas} \times V_{sample} \tag{4}$$

with $m_{corrected}$ the corrected weight (g), $m_{measured}$ the measured weight (g), ρ_{gas} the measuring gas density (g cm^{-3}) and V_{sample} the sample volume (cm^3).

The N_2 and CO_2 solubility in the membranes can be calculated with eqn (5):

$$S = \frac{C}{p} \tag{5}$$

with S the gas solubility (cm^3 (STP) cm^{-3} cmHg), C the quantity of adsorbed gas (cm^3 (STP) cm^{-3}) and p the pressure (cmHg).

2.4.7 Grand canonical Monte Carlo (GCMC) simulation of CO_2 adsorption behavior in MOF-808. The input structures for the GCMC simulations were obtained by optimizing the primitive unit cell of the different MOF-808 structures using CP2K.[32] The optimizations were performed at the PBE-D3(BJ)[33–35] level of theory, combined with Gaussian TZVP-MOLOPT[36] basis sets, a plane wave basis set with a cut-off of 800 Ry and a relative cut-off of 60 Ry, and Goedecker–Teter–Hutter (GTH) pseudopotentials,[37] allowing for a relaxation of both the atomic positions and the unit cell. The GCMC simulations were performed with RASPA,[38] using a fixed framework and rigid CO_2 and N_2 adsorbate molecules described by the TraPPE force field.[39] The atomic framework charges were derived from cluster calculations using the Minimal Basis Iterative Stockholder (MBIS) partitioning scheme[40] (see ESI† for more details), while the Lennard-Jones interaction parameters are taken from the DREIDING model[41] (except for zirconium, which was taken from UFF).[42,43] The temperature was set to 300 K. Each GCMC simulation consists of 10^7 cycles, with equal probabilities for translation, rotation, and (re)insertion moves. The first 10^5 cycles are regarded as equilibration steps and are not taken into account in any analysis.

The CO_2 enthalpy of adsorption can be determined from the GCMC simulations using eqn (6):

$$\Delta H_{ads} = \frac{\langle UN\rangle_\mu - \langle U\rangle_\mu \langle N\rangle_\mu}{\langle N^2\rangle_\mu - \langle N\rangle_\mu^2} - \langle U_{host}\rangle - \langle U_{guest}\rangle - k_B T \tag{6}$$

with U the total energy of the host framework and the adsorbed molecules, N the number of adsorbed molecules, $\langle U_{host}\rangle$ the average energy of the adsorbent, $\langle U_{guest}\rangle$ the average energy of the adsorbate molecule in the gas phase, k_B the Boltzmann constant, and T the absolute temperature.

$\langle\ldots\rangle_\mu$ denotes an average in the grand-canonical ensemble. As the host framework and the adsorbed molecules are described as rigid molecular systems, $\langle U_{host}\rangle = \langle U_{guest}\rangle = 0$.

The mixed-gas CO_2/N_2 selectivities of MOF–FA and MOF–TFA were determined from a separate set of GCMC simulations in which both CO_2 and N_2 molecules can be inserted or deleted. The mole fractions were set to 0.5, so that the selectivity can be calculated from the ratio of the number of adsorbed CO_2 molecules to the number of adsorbed N_2 molecules.

2.4.8 Gas permeation. Our in-house developed high-throughput gas separation set-up (HTGS) was used to examine the gas permeation behavior of the synthesized membranes. A detailed set-up description is given elsewhere.[44–46] HTGS allows simultaneous pure gas and mixed-gas testing of 16 membrane coupons at varying membrane temperatures and feed pressures. The active membrane area is 1.91 cm^2. CO_2 pure gas permeability and the CO_2/N_2 mixed-gas permeability and separation factor were measured for all membranes.

CO_2/N_2 mixed-gas separation factors (α^*) were measured by a GC analysis of the permeate composition. The ratio of the feed and permeate mole fraction of CO_2 and N_2 then renders the separation factor (eqn (7)):

$$\alpha^*_{CO_2/N_2} = \frac{y_{CO_2}/y_{N_2}}{x_{CO_2}/x_{N_2}} \quad (7)$$

where y_{CO_2} and y_{N_2} are the mole fractions of CO_2 and N_2 in the permeate, x_{CO_2} and x_{N_2} the mole fractions of gas CO_2 and N_2 in the feed. The ratio y_{CO_2}/y_{N_2} is determined from chromatogram peak areas of the permeate, while x_{CO_2}/x_{N_2} is determined by the feed settings.

Determination of the pure gas and mixed-gas permeabilities of CO_2 and N_2 was performed with a constant-volume–varying-pressure method. A pressure sensor (MKS Baratron) measures the change in pressure in a 75 cm^3 measuring cylinder while permeate gas is accumulated in the cylinder. The change in pressure as a function of time (dp/dt) is then used to calculated the permeability P (Barrer) with eqn (8). For pure gas measurements, the mole fraction of the gas in permeate and feed is 1.

$$P_{CO_2} = 10^{10} \times \frac{y_{CO_2} \times V \times V_m \times L}{x_{CO_2} \times p_{up} \times A \times R \times T} \times \frac{dp}{dt} \quad (8)$$

with P_i the gas permeability (Barrer), y_i the mole fraction of the component in the permeate, x_i the mole fraction of the component in the feed, V the downstream volume (cm^3), V_m the molar volume (22.414 L mol^{-1}), A the membrane permeation area (1.91 cm^2), L the membrane thickness (μm), T the operating temperature (K), p_{up} the upstream pressure (bar), R the gas constant (0.082 L atm mol^{-1} K^{-1}) and dp/dt the pressure increase (torr s^{-1}).

3 Results and discussion

3.1 Characterization of MOFs and membranes

Functionalization of the starting material MOF–FA does not change the crystal structure of the MOF since all its functionalized derivatives show a high degree of crystallinity (Fig. S1†), in good agreement with literature.[10,23,28] The variation in relative intensity between the large diffraction peak at 4.3° and the two smaller peaks at 8.3° and 8.7° can be attributed to the varying pore filling of the different MOFs.[47–49] Furthermore, post-synthetic functionalization does not affect the particle size nor morphology as confirmed by SEM (Fig. S2†). All MOFs have the same, lumped octahedral shape and a uniform, average MOF size of around 350 nm, originating from the starting material. A one-way analysis of variance (ANOVA) suggested no statistical difference in particle size between the MOFs (Tables S1 and S2†).

ATR-FTIR was used to further confirm the presence of the different ligands in the MOFs (Fig. 2). In all spectra, peaks situated at 453 cm^{-1} (Zr-μ_3-OH stretch) and 660 cm^{-1} (Zr-μ_3-O stretch) are associated with the Zr-oxide cluster.[20] Likewise, clearly distinguishable peaks are observed at 760 cm^{-1}, 1385 cm^{-1}, 1572 cm^{-1} and 1620 cm^{-1}, corresponding to vibrations of the BTC linker.[50] No signal was found between 1715–1750 cm^{-1}, which corresponds with the C=O stretch of uncoordinated ligands or BTC, hence indicating that the MOF pores do not contain physisorbed ligands.[50] Specific peaks belonging to the ligand were found for all samples. Additional bands for MOF–His are visible at 822 cm^{-1} and 1067 cm^{-1},

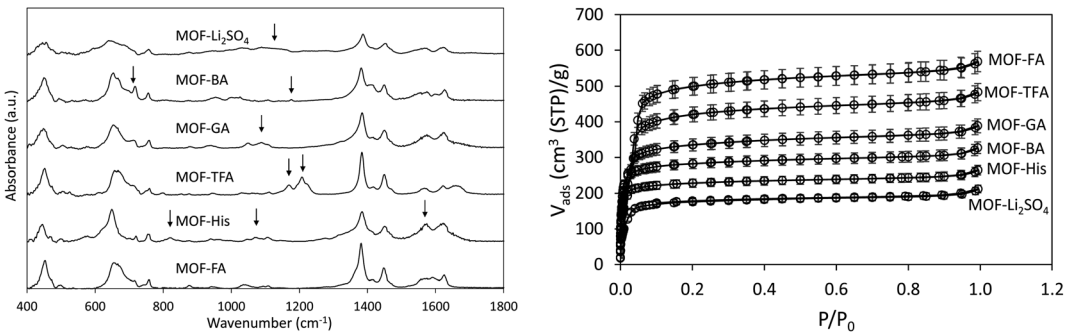

Fig. 2 ATR-FTIR spectrum (left) and N_2 adsorption isotherms at 77 K (right) of all MOFs.

resulting from mixed $-NH_3^+$ and –CH bending. Together with the higher relative absorbance of the signal at 1574 cm^{-1} ($-NH_3^+$ deformation), these absorptions suggests that histidine is present in its (partially) protonated form.[51–53] Specific absorption bands for MOF–TFA were recorded at 1170 and 1208 cm^{-1}, attributed to –CF symmetrical and anti-symmetrical stretch, respectively.[10] Signals for MOF–BA and MOF–GA were less pronounced as their characteristic bands mostly coincide with linker peaks. For MOF–BA, the signal at 718 cm^{-1} has a higher absorbance (associated with an increased out-of-plane –CH stretching of the benzene ring) while a new peak occurs at 1178 cm^{-1} (–CH bending ring).[54] MOF–GA shows a weak signal increase at 1000–1075 cm^{-1} (C–O stretch) but, most importantly, a broad signal at 3300 cm^{-1} due to –OH stretch (from GA, ethanol or water).[52] Finally, an enhanced absorbance intensity in the 900–1200 cm^{-1} region has previously been associated with effective SO_4 functionalization of MOF-808.[55]

Further confirmation of successful post-synthetic functionalization was performed with ^1H NMR and ^{19}F NMR (Fig. S4†). A higher ligand loading on the cluster was detected in the following order: MOF–TFA = MOF–His (3.3) > MOF–BA (3.2) > MOF–GA (2.3) > MOF–FA (2.2), as can be seen in Table 1. The difference in loading seems to roughly increase with decreasing pK_a of the carboxylic acid functional group (in water): TFA (0.23) > His (1.78) > GA (3.83) ~ FA (3.75).[56,57] A lower pK_a results in a larger concentration of deprotonated ligand at equal pH and thus a higher probability of incorporation in the MOF framework. MOF–BA deviates from this trend as it has the highest pK_a (4.20) but, at the same time, a loading of 3.2 BA per Zr_6 cluster. Due to the limited solubility of BA in water, BA functionalization took place in DMSO, whereas the other functionalizations were water-based, making it difficult to draw conclusions with regard to BA. None of the functional ligands had a cluster loading equal to the theoretical maximum of six, indicating that the remaining vacant sites were occupied by other charge compensating moieties (*i.e.* $-OH^-$, $-Cl^-$).[28]

CO_2 and N_2 physisorption experiments were conducted to determine characteristic MOF-808 parameters, such as pore volume and diameter, BET value and CO_2 uptake (Table 1). N_2 adsorption isotherms are given in Fig. 2. Substantial differences in BET surface area and pore volume exist between the functionalized MOFs. For the starting material MOF–FA, BET and pore volume correspond well with literature.[10,24,58] The BET surface area, pore volume and pore diameter (Fig. S5†) all decrease with increasing size of the ligand (MOF–TFA > MOF–GA > MOF–BA > MOF–His). Although Li_2SO_4 is considerably smaller in size than histidine and BA, MOF–Li_2SO_4 denotes the lowest BET and pore volume measured. As MOF–Li_2SO_4 retained its crystalline structure after functionalization, the low BET and pore volume suggest that the MOF pores might be partially blocked by salt deposition.

Furthermore, functionalization strongly affects the CO_2 uptake of the different MOFs as well (Fig. S6†). At 1000 mbar and 273 K, the MOF–FA starting material displays the highest uptake (65.9 cm^3 (STP) g^{-1}), indicating that functionalization reduced the uptake capacity of the MOFs. The CO_2 uptake follows a decreasing trend from MOF–FA > MOF–His > MOF–TFA > MOF–GA > MOF–BA > MOF–Li_2SO_4. However, only small differences in uptake (ranging from 48.1–55.2 cm^3 (STP) g^{-1}) are observed between the functionalized MOFs, except for MOF–Li_2SO_4, which loses more than 40% of uptake capacity compared to MOF–FA, further pointing towards the deposition of Li_2SO_4, blocking adsorption sites.[59] Besides the total CO_2 uptake capacity of the MOF, the initial slope of the CO_2 adsorption isotherm in the low-pressure region also reveals qualitative information about the MOF CO_2-philicity as it is governed by the sorption equilibrium constant (*b*-value).[60–63] Hence, adsorption in this pressure region is expected to correlate primarily with the MOF–CO_2 binding strength rather than with the specific surface area or pore volume. The slope in the lower pressure region (0–100 mbar, Fig. S7†) increases in the order MOF–BA < MOF–Li_2SO_4 < MOF–GA < MOF–FA ≈ MOF–His < MOF–TFA, which was further confirmed by the *b*-values obtained from the dual-site Langmuir model (Table S3†). The observed trends in CO_2 uptake and initial slope (*b*-value) indicate that MOF–TFA has the highest affinity for CO_2, although this is eventually not reflected in the highest total CO_2 uptake since the MOF starting material (*i.e.* MOF–FA) can adsorb up to 28% more CO_2. While this observation seems to contradict at first sight, it can be explained by the larger pore volume and surface area of MOF–FA. Furthermore, an almost linear CO_2 adsorption isotherm is observed for MOF–BA in the low-pressure region, which has previously been associated with a lack of high-affinity bindings sites in the MOF.[63,64] At higher pressures, the difference between the isotherms of the other MOFs is less pronounced (Fig. S6†).

Table 1 Average number of ligand molecules per Zr_6 cluster, pore volume (cm^3), pore diameter (Å), BET value (m^2 g^{-1}) and CO_2 uptake (cm^3 (STP) g^{-1}) at 273 K and 1000 mbar for all MOFs

	Ligands per Zr_6 cluster[a]	Pore volume (cm^3)	Pore diameter (Å)	BET value (m^2 g^{-1})	CO_2 uptake[b] (cm^3 (STP) g^{-1})
MOF–FA	2.2	0.76	18.4	2304	65.9
MOF–TFA	3.3	0.68	17.7	1946	51.2
MOF–GA	2.3	0.55	15.6	1421	50.9
MOF–BA	3.2	0.46	13.8	1119	48.1
MOF–His	3.4	0.37	10.9	901	55.2
MOF–Li_2SO_4	—	0.28	15.6	727	37.2

[a] As determined by NMR. [b] At 273 K and 1000 mbar.

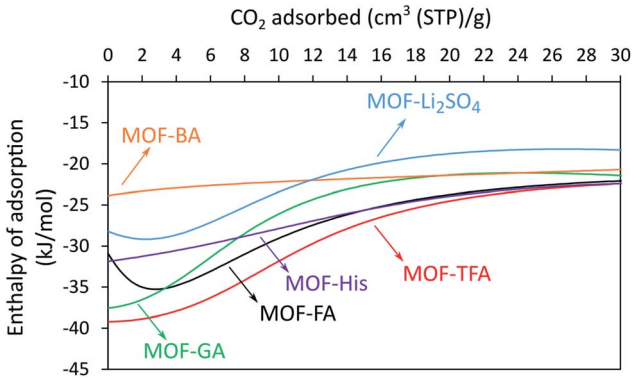

Fig. 3 Experimental CO_2 adsorption enthalpies as a function of CO_2 loading for all MOFs.

To obtain a more accurate and quantitative measure of the effect of functionalization on the MOF CO_2 affinity, the loading-dependent CO_2 Q_{st} was calculated for each MOF with the Clausius–Clapeyron method based on a dual-site Langmuir model (Fig. 3). Table S4† gives the MOF Q_{st} values at different loadings. At zero coverage, the diverse functionalizations result in a difference of ~15 kJ mol^{-1} between the highest Q_{st} (MOF–TFA, 39.2 kJ mol^{-1}) and the lowest Q_{st} (MOF–BA, 23.9 kJ mol^{-1}). The curve of the graphs of MOF–FA, MOF–TFA, MOF–GA, MOF–Li_2SO_4 and (to a lesser extent) MOF–His all display a substantial Q_{st} reduction with increasing coverage. Comparable behavior has been associated with the saturation of high-affinity gas binding sites inside the MOF.[65,66] The minima in Q_{st} observed for MOF–FA and MOF–Li_2SO_4 are believed to be an artefact of the model's limited number of temperature data points. For the higher coverages, the Q_{st} appears to approach a pseudo-constant value of roughly 21–22 kJ mol^{-1}, with only small differences in the adsorption enthalpy between the MOFs, corresponding with the occupation of the low-affinity adsorption sites in the isostructural MOFs.[66] The change in Q_{st} of MOF–BA remains rather limited, suggesting a larger binding site homogeneity (as was also concluded from the CO_2 adsorption isotherm). CO_2 Q_{st} values in this work are comparable to the Q_{st} values reported in literature for similar MOFs. Plonka *et al.* found a Q_{st} of 32 kJ mol^{-1} for FA modulated MOF-808, well in line with our findings.[67] Very similar values were reported for perfluoroalkane functionalized NU-1000 (which contains the same Zr_6 cluster as MOF-808) with $Q_{st,0}$ between 20 and 34 kJ mol^{-1} while the pristine NU-1000 gave a CO_2 $Q_{st,0}$ of 17 kJ mol^{-1}.[66,68] For UiO-66, CO_2 adsorption enthalpies at zero coverage vary between 26 and 38 kJ mol^{-1}, depending on the type of functionalization.[69,70] The highest Q_{st} in this work was noted for MOF–TFA over the entire range of CO_2 loading.

SEM cross-sections of the MMMs show that the different MOFs are homogeneously incorporated in the polymer matrix, without noticeable differences between the samples (Fig. S12 and S13†). TGA measurements revealed that thermal stability of the membranes after incorporation of the MOF remained at the same level for all MOFs (Fig. S14†). In addition, all MMMs contained between 8 and 10 wt% MOF. An enhanced T_g was observed for all MMMs compared to the unfilled Matrimid membrane (T_g = 312 °C), indicating polymer rigidification at the polymer/particle interphase to a certain extent (Fig. S15†). Only small variations in T_g can be observed between the MMMs, suggesting a very similar degree of polymer rigidification for the different MMMs. All MMMs have a T_g between 320 and 322 °C with an exception of MMM–FA (T_g = 324 °C). This is most probably a result of the slightly higher weight percentage of MOF–FA in the membrane as can be observed from TGA data. Finally, N_2 and CO_2 sorption were measured for all membranes (Fig. 4) and the corresponding solubility values were calculated in Table S5.† With increasing pressure, CO_2 sorption in the membranes clearly increases from Matrimid < MMM–GA < MMM–His < MMM–BA < MMM–FA < MMM–Li_2SO_4 < MMM–TFA. On the other hand, the N_2 sorption data are more difficult to analyze as only small differences between the samples can be

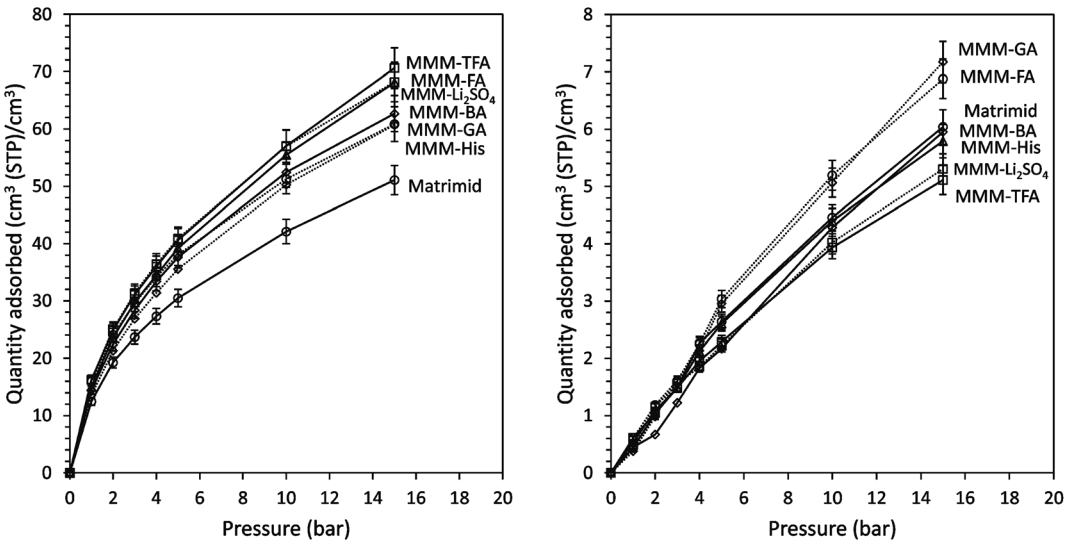

Fig. 4 CO_2 (left) and N_2 (right) sorption in the Matrimid reference membrane and all MMMs.

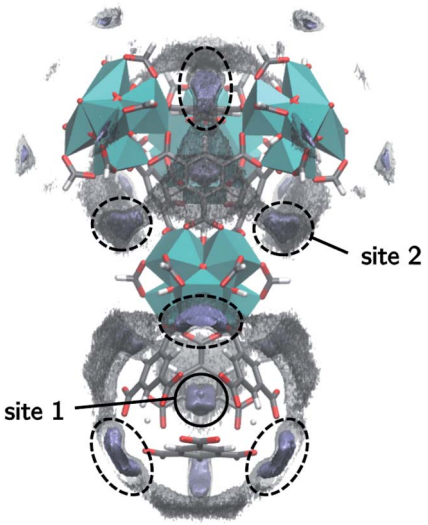

Fig. 5 Two isosurfaces of the density of MOF–FA from GCMC simulations at 2 bar. The high density isosurface of sites 1 and 2 is shown in iceblue and a lower density isosurface is shown to encapsulate the metal cluster.

noticed. In general, a strong improvement in solubility selectivity is observed for FA, BA, TFA and Li_2SO_4 functionalized MOF-808 compared to the pristine Matrimid membrane while MOF–GA and MOF–His only modestly affect the CO_2/N_2 solubility selectivity. At 5 bar, the highest solubility selectivities are measured for MOF–TFA (17.8) and MOF–Li_2SO_4 (18.4), which represent an 54% and 59% increase compared to Matrimid, respectively.

3.2 Computational MOF characterization

GCMC simulations were applied on MOF–FA and MOF–TFA to acquire the MOF CO_2 adsorption sites, adsorption enthalpy and mixed-gas CO_2/N_2 adsorption selectivity. Additionally, the CO_2 adsorption isotherms were simulated and are available in Fig. S9.†

The adsorption densities of the CO_2 molecules at different pressure for MOF–FA are displayed in Fig. 6, in which the primitive unit cell was expanded to the conventional cubic cell for ease of interpretation (Fig. S10†). At low pressures, the CO_2 molecules are primarily located within the cages formed by the four benzene rings of the linker, yielding a square grid of adsorption sites when viewing MOF-808 along the *c*-axis (marked as site 1 in Fig. 5 and 6). A second type of adsorption

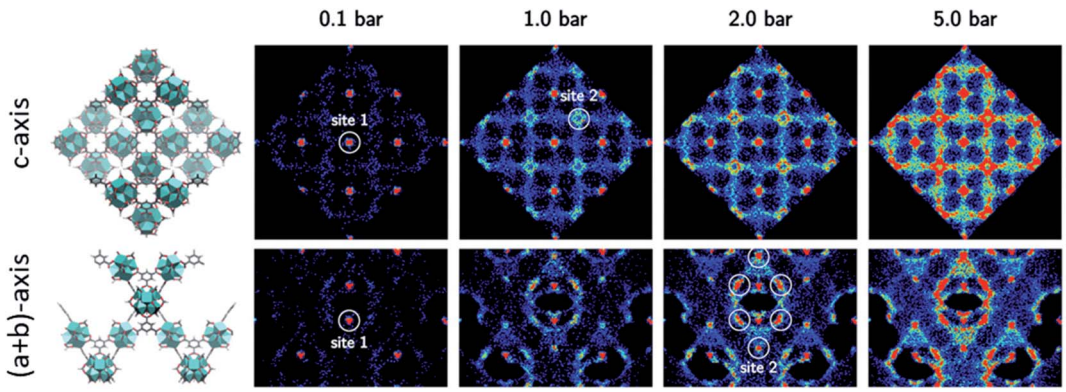

Fig. 6 Density of the adsorbed CO_2 molecules in MOF–FA at 300 K projected on a plane orthogonal to the c-axis and the (*a* + *b*)-axis of the conventional unit cell. The CO_2 molecules are represented by the positions of the carbon atoms.

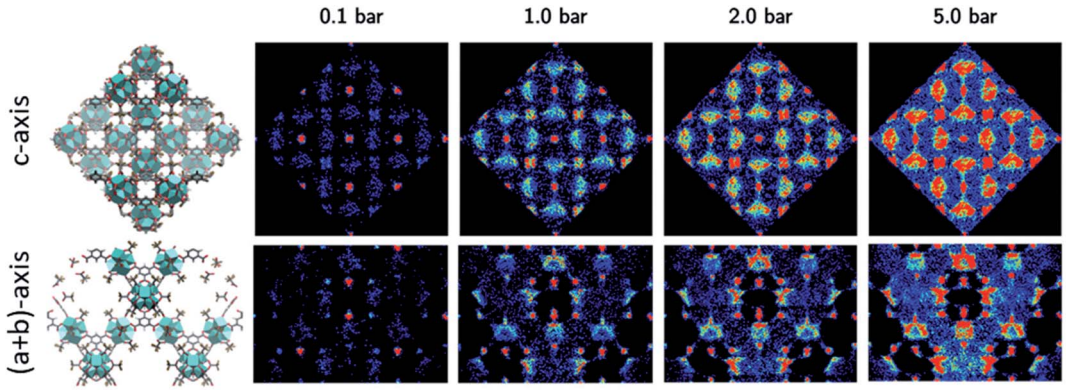

Fig. 7 Density of the adsorbed CO_2 molecules in MOF–TFA at 300 K projected on a plane orthogonal to the *c*-axis and the (*a* + *b*)-axis of the conventional unit cell. The CO_2 molecules are represented by the positions of the carbon atoms.

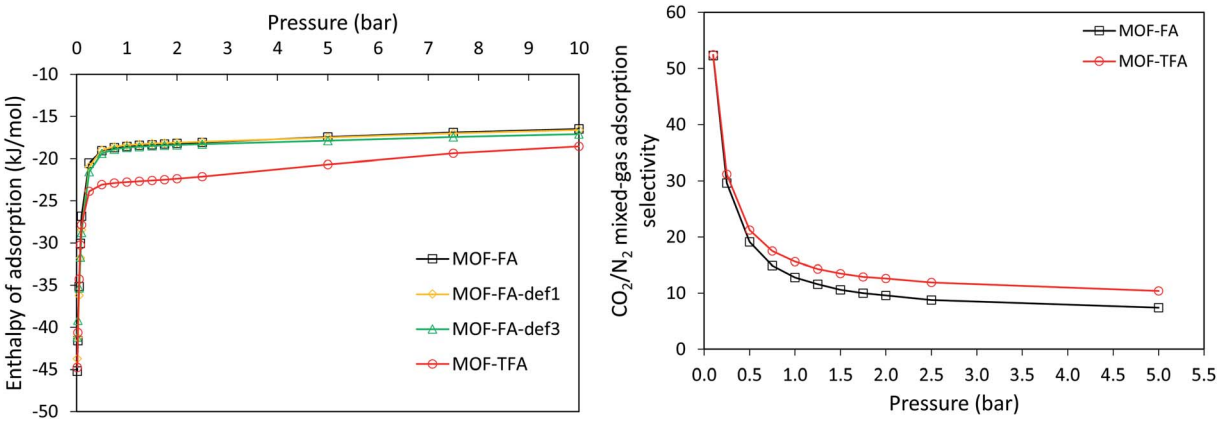

Fig. 8 Simulated CO_2 adsorption enthalpies for MOF–FA, MOF–TFA and MOF–FA with 1 and 3 defects, respectively (left). Simulated mixed-gas adsorption CO_2/N_2 selectivities for MOF–FA and MOF–TFA (right).

sites that gain importance with increasing pressure are located in between the zirconium clusters, covering the open sides of the linkers (marked as site 2 in Fig. 5 and 6).[67] At higher pressures, the linkers eventually become fully encapsulated by CO_2 with increasing pressure.

Although the adsorption sites for MOF–TFA are similar, the filling pattern is different due to the presence of the TFA functional groups, which results in a higher degree of localization of the adsorbed CO_2 molecules (Fig. 7). After filling the tetragonal cages at the lowest pressures, the CO_2 molecules further adsorb onto the linkers. In contrast to MOF–FA, the adsorption sites located above the benzene rings of the linkers are also significantly occupied for mid-range pressures, implying that the surrounding TFA functionalizations enhance the adsorption energy of these sites (more negative adsorption enthalpy).

This is also confirmed by the calculated enthalpies of CO_2 adsorption for both MOFs (Fig. 8, also Table S6†). At the lowest pressures, the enthalpy of adsorption is completely dominated by the host–adsorbate interaction. Initially, the enthalpy values for MOF–FA and MOF–TFA are hence very similar as CO_2 first adsorbs in the tetragonal cages (site 1). Once adsorption sites on the linker molecules (site 2) become relevant, MOF–TFA shows significantly lower adsorption enthalpies (stronger host–adsorbate interaction), in good agreement with the experimentally determined isosteric CO_2 adsorption enthalpy. A more moderate difference is observed at higher pressures as the adsorbate–adsorbate interactions also start to contribute to the adsorption enthalpy. Eventually, this is reflected in higher mixed-gas CO_2/N_2 selectivities for MOF–TFA, confirming the experimental trends. Finally, the influence of open metal site defects (*i.e.* as a result of missing modulators) on the enthalpy of adsorption was also investigated for MOF–FA, by creation of a MOF–FA structure with 1 defect (MOF–FA-def1) and 3 defects (MOF–FA-def3), respectively (Fig. S11 and Table S6†). As can be seen in Fig. 8, no difference in CO_2 adsorption enthalpy is observed between MOF–FA and MOF–FA-def1 while the CO_2 adsorption enthalpy of MOF–FA-def3 is slightly lower than that of MOF–FA but still significantly higher than the adsorption enthalpy of MOF–TFA, indicating that the sole effect of defects on the CO_2 adsorption is rather limited in MOF–FA.

3.3 Gas permeation

CO_2 permeability of the mixed-gas experiments with 15%/85% v/v and 50%/50% v/v CO_2/N_2 feed compositions and of the CO_2 pure gas experiment is given in Fig. 9. All MMMs show a significantly higher CO_2 permeability for all feed compositions compared to the pristine Matrimid membrane, owing to the incorporation of

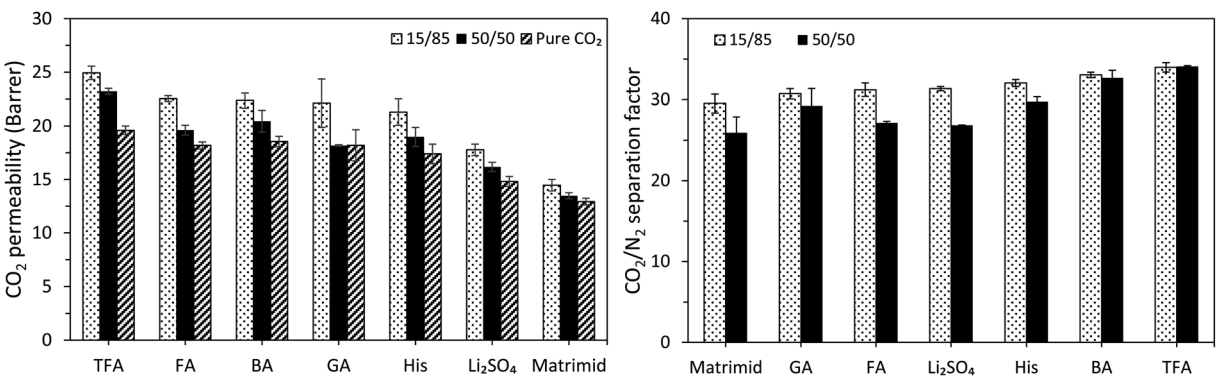

Fig. 9 CO_2 permeability (left) and CO_2/N_2 separation factor (right) for the 15%/85% v/v and 50%/50% v/v mixed-gas CO_2/N_2 experiment and the CO_2 pure gas experiment of all membranes. Gas filtrations were performed at 30 °C and 5 bar feed pressure. All MMMs contain 10 wt% MOF.

Table 2 Correlation coefficients between MOF-808 parameters (CO_2 uptake at 50 and 1000 mbar and Q_{st} at a coverage of 0, 15, 30 cm^3 (STP) g^{-1}) and the corresponding MMM parameters (α* at 15%/85% v/v and 50%/50% v/v CO_2/N_2 feed, and CO_2 permeabilities for 15%/85% v/v and 50%/50% v/v CO_2/N_2 feed and the pure CO_2 feed ($P_{100/0}$)). Strong correlations are indicated in bold and weak correlations in italics. Intermediate correlations have no special markings

	CO_2 uptake (50 mbar)	CO_2 uptake (1000 mbar)	BET surface area	Pore volume	$Q_{st,0}$	$Q_{st,15}$	$Q_{st,30}$
$\alpha^*_{15/85}$	*0.079*	*0.053*	*0.123*	*0.173*	*0.056*	0.414	*0.291*
$\alpha^*_{50/50}$	*0.010*	*0.106*	*0.126*	*0.230*	*0.222*	0.368	0.423
$P_{15/85}$	0.431	0.658	0.722	**0.800**	0.513	0.756	**0.834**
$P_{50/50}$	0.532	0.558	0.681	0.733	0.473	**0.844**	0.793
$P_{100/0}$	0.352	0.665	0.622	0.716	0.433	0.715	**0.866**

the MOF.[71,72] For the 15%/85% v/v CO_2/N_2, the 50%/50% v/v CO_2/N_2 and the pure CO_2 data, respectively, the smallest permeability increase was observed for MMM–Li_2SO_4 (+23%, +20%, +15%) while the most substantial increase was recorded for MMMs containing MOF–TFA (+52%, +72%, +72%) as a result of a substantially increased CO_2 solubility upon incorporation of the TFA functionalized MOF (+33%). The low MMM–Li_2SO_4 permeability can be linked to the above-mentioned pore blockage by Li_2SO_4 deposition. Furthermore, a similar trend can be seen for the various feed conditions with the CO_2 permeability increasing in the order Matrimid < MMM–Li_2SO_4 < MMM–His ≈ MMM–GA ≈ MMM–BA ≈ MMM–FA < MMM–TFA. Finally, the CO_2 permeability is reduced when the CO_2 content in the feed is increased from 15% to 50% and eventually to 100%. A similar trend was observed for UiO-66-NH_2 MMMs based on various fluorinated polyimides.[11,19,73] These observations are in line with the dual-mode sorption model, which predicts saturation of polymer excess free volume elements at elevated CO_2 pressure, resulting in a lowered CO_2 solubility.[74,75]

The CO_2/N_2 separation factors of Matrimid (Fig. 9) for the 15%/85% v/v (29.5) and the 50%/50% v/v feed (25.9) are similar to literature.[76,77] In general, incorporation of the functionalized MOFs leads to a small enhancement in CO_2/N_2 separation factor for both feed mixtures compared to the pristine Matrimid membrane, but only small differences can be noticed between the MMMs. DSC measurements confirmed a similar increase in T_g for all MMMs. This indicates a certain (and similar) degree of polymer rigidification at the polymer/particle interface, thus (partially) explaining the elevated MMM separation factor. In addition, since no differences in particle morphology or particle size were observed with SEM (all MOFs were synthesized starting from the same MOF–FA batch), it is reasonable to assume that polymer rigidification is comparable for all MMMs. Similar to the permeability measurements, MOF–TFA causes the largest improvement of the separation factor of all MOFs, while MOF–GA, MOF–Li_2SO_4 and MOF–FA do not significantly affect the 15%/85% v/v and 50%/50% v/v separation factor. Functionalization with TFA (+9%, +25%) results in the best performance (compared to MMM–FA), which can be explained by the improved CO_2/N_2 selectivity for MOF–TFA (as was confirmed by the GCMC simulations) and the resulting increasing in solubility selectivity for MMM–TFA. As mentioned earlier, it is believed that the strongly polarized C–F bonds in MOF–TFA and the consequent higher CO_2 affinity are at the base of the good separation factor for MMM–TFA.[10] This was confirmed by both experimental and simulated CO_2 adsorption enthalpies, which were significantly lower (stronger MOF–CO_2 interaction) upon functionalization with TFA and eventually resulted in an enhanced CO_2/N_2 mixed-gas adsorption selectivity for MOF–TFA compared to MOF–FA (Fig. 8). For the BA functionalized MOF, MMM–BA probably profits from enhanced π–π interaction between phenyl groups at the MOF surface and aromatic moieties of the polymer chains, which has previously been reported to improve polymer–MOF compatibility and, as a result, the separation factor.[78] It can be hypothesized that a higher CO_2 Q_{st} might lead to a higher selectivity for the MMM based on MOF–TFA, but observations for MOF–BA (with the lowest $Q_{st,0}$ but second highest α*) contradict this. Finally, a lowered CO_2/N_2 selectivity for the 50%/50% v/v feed is expected based on the dual-sorption model as the N_2 partial pressure is reduced (higher N_2 permeability), while the CO_2 partial pressure is enhanced (lower CO_2 permeability).[75]

3.4 Correlation of MOF parameters with membrane CO_2 permeation

Overall, the effect of ligand type on the MMM CO_2 permeability and CO_2/N_2 separation factor strongly varies when compared to the MOF–FA starting material. Only functionalization with TFA and Li_2SO_4 causes the MMM permeability to change significantly while improved separation factors with respect to MOF–FA are only observed for BA and TFA functionalization. To quantify the relationship between the examined MOF properties and the MMM permeation behavior, correlation coefficients between these parameters have been calculated in Table 2. Results were interpreted based on statistic guidelines defined by Ross *et al.*[79] Correlation coefficients lower than 0.30 are considered as weak correlations, between 0.30 and 0.80 as moderate and higher than 0.80 as strong.

The conventional MOF parameters (BET surface area and pore volume) display a moderate linear correlation with the obtained permeabilities. This seems reasonable, owing to the positive relationship between gas diffusivity and MMM free volume.[75] In addition, a weak correlation is observed between these parameters and the CO_2/N_2 separation factor. Unexpectedly, also CO_2 uptake in both the low (at 50 mbar) and high (at 1000 mbar) pressure region correlates very poorly with both separation factors, while only moderate correlations were noted

with permeability in 15%/85%, 50%/50% v/v and pure CO_2 feed. This strongly contrasts with literature, where a high CO_2 uptake is very frequently used to explain MMM permeation observations.[27,80] The correlation of Q_{st} on one hand with CO_2 permeability and CO_2/N_2 separation factor on the other hand is less straightforward to interpret. The adsorption enthalpy at zero coverage ($Q_{st,0}$) shows moderate correlation with the CO_2 permeabilities, comparable to the CO_2 uptake values. Similarly, only weak correlations are observed for $Q_{st,0}$ and the different separation factors. Interestingly, strong correlations are observed between $Q_{st,15}$ and $Q_{st,30}$ on one hand and $P_{15/85}$, $P_{50/50}$ and $P_{100/0}$ on the other hand while correlation coefficients of $Q_{st,15}$ and $Q_{st,30}$ with the $\alpha^*_{15/85}$ and $\alpha^*_{50/50}$ are higher than for CO_2 uptake but are still considered only moderate. As such, Q_{st} can be considered as the most effective predictor for MMM CO_2 permeability amongst all MOF parameters.

A possible explanation for the difference in correlation strength of the Q_{st} at low loading and the ones at high loading might be found in the existence of mobile and immobile gas species in the membrane.[81] $Q_{st,0}$ represents the adsorption enthalpy of the high affinity sorption sites in the MOF and can possibly be linked to the tetragonal cages, which are the primary CO_2 sorption sites (marked as site 1 in Fig. 6 and 7) at very low CO_2 pressure. These sites correspond with highly negative CO_2 adsorption enthalpies (very strong MOF–CO_2 interaction) and the highest CO_2/N_2 mixed-gas adsorption selectivity values observed (up to 60, Fig. 8). Moreover, they are present in both MOF–FA and MOF–TFA (and, by extension, in all functionalized MOF-808 samples), explaining the very similar enthalpy and selectivity values for both MOFs at low CO_2 pressures. At relatively higher CO_2 pressures (starting from 0.25 bar in Fig. 8), the GCMC simulations show substantial differences in adsorption enthalpy and CO_2/N_2 adsorption selectivities between MOF–FA and MOF–TFA caused by the increased influence of the second type of adsorption sites (marked as site 2 in Fig. 6 and 7). It can thus be hypothesized that these sites (partially) immobilize gas molecules through (too) strong binding interaction[26] and thus do not (or to a lesser extent) contribute to gas permeation through the membrane. Although this hypothesis should be proven by performing time-lag experiments, it would explain the observed difference in correlation coefficients for $Q_{st,0}$ and $Q_{st,30}$.[81]

As the overall gas permeability through the MMM is a net result of both MOF and polymer properties and their mutual interactions, it is not unexpected that none of the MOF parameters can predict the trends in MMM permeability one-on-one. Nonetheless, the unanticipated lack of correlation for CO_2 permeability with CO_2 uptake and its strong correlation with $Q_{st,15}$ and $Q_{st,30}$ once more underline the difficulty to formulate strong and general guidelines to steer MMM design and, more importantly, the need for more research aiming at finding consistent relationships between MOF and MMM structures and ultimate membrane performance.

4 Conclusions

An attempt was made to fundamentally correlate MOF-808 parameters with the CO_2/N_2 separation performance indicators of the corresponding MMMs. More specifically, MOF CO_2 uptake, CO_2 Q_{st} at different CO_2 loading, pore volume and BET surface area were correlated with the MMM CO_2/N_2 separation factor and CO_2 permeability under varying feed conditions. Post-synthetic functionalization of FA modulated MOF-808 with different ligands (*i.e.* TFA, BA, GA, histidine and Li_2SO_4) proved to be a successful tool to influence this set of MOF parameters, leading to a broad range of systematically varying parameter values for BET surface area, pore volume, CO_2 uptake and CO_2 Q_{st}. For the different MOF-808 MMMs tested in this work, MOF CO_2 uptake was a poor predictor for MMM performance, showing a very weak correlation with CO_2/N_2 separation factor and only moderate correlation with CO_2 permeability. This is in contrast to literature where CO_2 uptake is one of the dominant factors used to explain MMM separation behavior. The loading-dependent CO_2 Q_{st} correlates substantially better with the membrane performance indicators than the CO_2 uptake. Correlation coefficients of $Q_{st,15}$ and $Q_{st,30}$ with the separation factor were higher than for CO_2 uptake, but were still considered only moderate. A strong correlation was however found between $Q_{st,15}$ and $Q_{st,30}$ on one hand and $P_{15/85}$, $P_{50/50}$ and $P_{0/100}$ on the other hand, indicating that Q_{st} can be considered as the most effective predictor for MMM CO_2 permeability amongst the MOF parameters. Interestingly, Q_{st} at zero coverage failed to show a strong correlation with the MMM performance indicators. GCMC simulations on MOF–FA and MOF–TFA revealed the existence of 2 types of adsorption sites in MOF-808. The first type of adsorption type is independent of cluster functionalization (*e.g.* TFA instead of FA) and corresponds with the tetragonal 'linker' cage, resulting in very strong MOF–CO_2 interaction (highly negative adsorption enthalpies) even at low CO_2 pressures while the second type of adsorption site was shown to be susceptible to TFA functionalization. Finally, the existence of different adsorption sites with varying adsorption enthalpies was linked to the observed difference in correlation coefficients for $Q_{st,0}$ and $Q_{st,30}$ with CO_2 permeability.

Conflicts of interest

There are no conflicts to declare.

Acknowledgements

R. T., N. V. V. and A. L. acknowledge the FWO for their support through a(n) (SB-)PhD fellowship (1S63317N, 1S32917N and 11D2220N). A. L. and V. V. S. would also like to thank the Research Board of Ghent University (BOF) for their support and the European Union's Horizon 2020 Research and Innovation Programme [ERC Consolidator Grant Agreement 647755 – DYNPOR (2015–2020)] for the received funding. The computational resources (Stevin Supercomputer Infrastructure) and services used in this work were provided by the VSC (Flemish Supercomputer Center), funded by Ghent University, FWO and the Flemish Government – Department EWI.

References

1 B. Seoane, J. Coronas, I. Gascon, M. E. Benavides, O. Karvan, J. Caro, F. Kapteijn and J. Gascon, Metal–Organic Framework Based Mixed Matrix Membranes: A Solution for Highly Efficient CO_2 Capture?, *Chem. Soc. Rev.*, 2015, **44**, 2421–2454, DOI: 10.1039/C4CS00437J.

2 M. Rezakazemi, A. Ebadi Amooghin, M. M. Montazer-Rahmati, A. F. Ismail and T. Matsuura, State-of-the-Art Membrane Based CO_2 separation Using Mixed Matrix Membranes (MMMs): An Overview on Current Status and Future Directions, *Prog. Polym. Sci.*, 2014, **39**(5), 817–861, DOI: 10.1016/j.progpolymsci.2014.01.003.

3 K. Vanherck, G. Koeckelberghs and I. F. J. Vankelecom, Crosslinking Polyimides for Membrane Applications: A Review, *Prog. Polym. Sci.*, 2013, **38**(6), 874–896, DOI: 10.1016/j.progpolymsci.2012.11.001.

4 C. Z. Liang, T.-S. Chung and J.-Y. Lai, A Review of Polymeric Composite Membranes for Gas Separation and Energy Production, *Prog. Polym. Sci.*, 2019, **97**, 101141, DOI: 10.1016/j.progpolymsci.2019.06.001.

5 H. Li, K. Haas-Santo, U. Schygulla and R. Dittmeyer, Inorganic Microporous Membranes for H_2 and CO_2 Separation—Review of Experimental and Modeling Progress, *Chem. Eng. Sci.*, 2015, **127**, 401–417, DOI: 10.1016/j.ces.2015.01.022.

6 M. Tsapatsis, Toward High-Throughput Zeolite Membranes, *Science*, 2011, **334**(November), 767–769, DOI: 10.1126/science.1205957.

7 Q. Qian, W. S. Chi, G. Han and Z. P. Smith, Impact of Post-Synthetic Modification Routes on Filler Structure and Performance in Metal–Organic Framework-Based Mixed-Matrix Membranes, *Ind. Eng. Chem. Res.*, 2020, **59**, 5432–5438, DOI: 10.1021/acs.iecr.9b04820.

8 W. S. Chi, B. J. Sundell, K. Zhang, D. J. Harrigan, S. C. Hayden and Z. P. Smith, Mixed-Matrix Membranes Formed from Multi-Dimensional Metal–Organic Frameworks for Enhanced Gas Transport and Plasticization Resistance, *ChemSusChem*, 2019, **02139**, 2355–2360, DOI: 10.1002/cssc.201900623.

9 S. Shahid and K. Nijmeijer, Performance and Plasticization Behavior of Polymer–MOF Membranes for Gas Separation at Elevated Pressures, *J. Membr. Sci.*, 2014, **470**, 166–177, DOI: 10.1016/j.memsci.2014.07.034.

10 R. Thür, N. Van Velthoven, V. Lemmens, M. Bastin, S. Smolders, D. De Vos and I. F. J. Vankelecom, Modulator-Mediated Functionalization of MOF-808 as a Platform Tool to Create High-Performance Mixed-Matrix Membranes, *ACS Appl. Mater. Interfaces*, 2019, **11**, 44792–44801, DOI: 10.1021/acsami.9b19774.

11 M. Z. Ahmad, T. A. Peters, N. M. Konnertz, T. Visser, C. Téllez, J. Coronas, V. Fila, W. M. de Vos and N. E. Benes, High-Pressure CO_2/CH_4 Separation of Zr-MOFs Based Mixed Matrix Membranes, *Sep. Purif. Technol.*, 2020, **230**(June 2019), 115858, DOI: 10.1016/j.seppur.2019.115858.

12 G. Dong, H. Li and V. Chen, Challenges and Opportunities for Mixed-Matrix Membranes for Gas Separation, *J. Mater. Chem. A*, 2013, **1**(15), 4610–4630, DOI: 10.1039/C3TA00927K.

13 M. Van Essen, E. Montrée, M. Houben, Z. Borneman and K. Nijmeijer, Magnetically Aligned and Enriched Pathways of Zeolitic Imidazolate Framework 8 in Matrimid Mixed Matrix Membranes for Enhanced CO_2 Permeability, *Membranes*, 2020, **10**(7), 155.

14 T. Rodenas, M. Van Dalen, E. García-Pérez, P. Serra-Crespo, B. Zornoza, F. Kapteijn and J. Gascon, Visualizing MOF Mixed Matrix Membranes at the Nanoscale: Towards Structure–Performance Relationships in CO_2/CH_4 Separation Over NH2-MIL-53(Al)@PI, *Adv. Funct. Mater.*, 2014, **24**, 249–256, DOI: 10.1002/adfm.201203462.

15 A. Ozcan, R. Semino, G. Maurin and A. O. Yazaydin, Modeling of Gas Transport through Polymer/MOF Interfaces: A Microsecond-Scale Concentration Gradient-Driven Molecular Dynamics Study, *Chem. Mater.*, 2020, **32**, 1288–1296, DOI: 10.1021/acs.chemmater.9b04907.

16 Z. Kang, Y. Peng, Z. Hu, Y. Qian, C. Chi, L. Y. Yeo, L. Tee and D. Zhao, Mixed Matrix Membranes Composed of Two-Dimensional Metal–Organic Framework Nanosheets for Pre-Combustion CO_2 Capture: A Relationship Study of Filler Morphology versus Membrane, *J. Mater. Chem. A*, 2015, **3**, 20801–20810, DOI: 10.1039/c5ta03739e.

17 K. Chen, K. Xu, L. Xiang, X. Dong, Y. Han, C. Wang, L. Sun and Y. Pan, Enhanced CO_2/CH_4 Separation Performance of Mixed-Matrix Membranes through Dispersion of Sorption-Selective MOF Nanocrystals, *J. Membr. Sci.*, 2018, **563**(March), 360–370, DOI: 10.1016/j.memsci.2018.06.007.

18 Y. Cheng, Y. Ying, L. Zhai, G. Liu, J. Dong, Y. Wang, M. P. Christopher, S. Long, Y. Wang and D. Zhao, Mixed Matrix Membranes Containing MOF@COF Hybrid Fillers for Efficient CO_2/CH_4 Separation, *J. Membr. Sci.*, 2019, **573**(November 2018), 97–106, DOI: 10.1016/j.memsci.2018.11.060.

19 Q. Qian, A. X. Wu, W. S. Chi, P. A. Asinger, S. Lin, A. Hypsher and Z. P. Smith, Mixed-Matrix Membranes Formed from Imide-Functionalized UiO-66-NH2 for Improved Interfacial Compatibility, *ACS Appl. Mater. Interfaces*, 2019, **11**, 31257–31269, DOI: 10.1021/acsami.9b07500.

20 R. Thür, N. Van Velthoven, S. Slootmaekers, J. Didden, R. Verbeke, S. Smolders, W. Egger, M. Dickmann, D. De Vos and I. F. Vankelecom, J. Bipyridine-Based UiO-67 as Novel Filler in Mixed-Matrix Membranes for CO_2-Selective Gas Separation, *J. Membr. Sci.*, 2019, **576**(15 April 2019), 78–87, DOI: 10.1016/j.memsci.2019.01.016.

21 G. Yu, Y. Li, Z. Wang, T. Xiaoteng, G. Zhu and X. Zou, Mixed Matrix Membranes Derived from Nanoscale Porous Organic Frameworks for Permeable and Selective CO_2 Separation, *J. Membr. Sci.*, 2019, **591**(August), 117343, DOI: 10.1016/j.memsci.2019.117343.

22 C. Jia, F. G. Cirujano, B. Bueken, B. Claes, D. Jonckheere, K. M. Van Geem and D. De Vos, Geminal Coordinatively Unsaturated Sites on MOF-808 for the Selective Uptake of Phenolics from a Real Bio-Oil Mixture, *ChemSusChem*, 2019, **101**, 1256–1266, DOI: 10.1002/cssc.201802692.

23 N. Van Velthoven, M. Henrion, J. Dallenes, A. Krajnc, A. L. Bugaev, P. Liu, S. Bals, A. V. Soldatov and D. E. De Vos, S,O-Functionalized Metal–Organic Frameworks as Heterogeneous Single-Site Catalysts for the Oxidative Alkenylation of Arenes via C–H Activation, *ACS Catal.*, 2020, **10**, 5077–5085, DOI: 10.1021/acscatal.0c00801.

24 H. Reinsch, S. Waitschat, S. M. Chavan, K. P. Lillerud and N. Stock, A Facile "Green" Route for Scalable Batch Production and Continuous Synthesis of Zirconium MOFs, *Eur. J. Inorg. Chem.*, 2016, **2016**(27), 4490–4498, DOI: 10.1002/ejic.201600295.

25 D. F. Sanders, Z. P. Smith, R. Guo, L. M. Robeson, J. E. McGrath, D. R. Paul and B. D. Freeman, Energy-Efficient Polymeric Gas Separation Membranes for a Sustainable Future: A Review, *Polymer*, 2013, **54**(18), 4729–4761, DOI: 10.1016/j.polymer.2013.05.075.

26 M. Galizia, W. S. Chi, Z. P. Smith, T. C. Merkel, R. W. Baker and B. D. Freeman, Polymers and Mixed Matrix Membranes for Gas and Vapor Separation: A Review and Prospective Opportunities, *Macromolecules*, 2017, **50**, 7809–7843, DOI: 10.1021/acs.macromol.7b01718.

27 Q. Qian, P. A. Asinger, M. J. Lee, G. Han, K. M. Rodriguez, S. Lin, F. M. Benedetti, A. X. Wu, W. S. Chi and Z. P. Smith, MOF-Based Membranes for Gas Separations, *Chem. Rev.*, 2020, **120**(16), 8161, DOI: 10.1021/acs.chemrev.0c00119.

28 J. Baek, B. Rungtaweevoranit, X. Pei, M. Park, S. C. Fakra, Y.-S. Liu, R. Matheu, S. A. Alshmimri, S. Alshehri, C. A. Trickett, *et al.*, Bioinspired Metal–Organic Framework Catalysts for Selective Methane Oxidation to Methanol, *J. Am. Chem. Soc.*, 2018, **140**, 18208–18216, DOI: 10.1021/jacs.8b11525.

29 F. Rouquerol, J. Rouquerol and K. Sing, *Adsorption by Powders and Porous Solids*, Academic Press, San Diego, 11th edn, 1999.

30 K. S. Walton and R. Q. Snurr, Applicability of the BET Method for Determining Surface Areas of Microporous Metal–Organic Frameworks, *J. Am. Chem. Soc.*, 2007, **129**(27), 8552–8556, DOI: 10.1021/ja071174k.

31 H. J. Park and M. P. Suh, Enhanced Isosteric Heat, Selectivity and Uptake Capacity of CO_2 Adsorption in a Metal–Organic Framework by Impregnated Metal Ions, *Chem. Sci.*, 2013, **4**(3), 685–690, DOI: 10.1039/c2sc21253f.

32 J. Hutter, M. Iannuzzi, F. Schiffmann and J. Vande Vondele, Cp2k: Atomistic Simulations of Condensed Matter Systems, *Wiley Interdiscip. Rev.: Comput. Mol. Sci.*, 2013, **4**(1), 15–25.

33 J. P. Perdew, K. Burke and M. Ernzerhof, Generalized Gradient Approximation Made Simple, *Phys. Rev. Lett.*, 1996, 77(3), 3865–3868.

34 S. Grimme, J. Antony, S. Ehrlich and H. Krieg, A Consistent and Accurate Ab Initio Parametrization of Density Functional Dispersion Correction (DFT-D) for the 94 Elements H-Pu, *J. Phys. Chem.*, 2010, **132**, 154104.

35 S. Grimme, S. Ehrlich and L. Goerigk, Effect of the Damping Function in Dispersion Corrected Density Functional Theory, *J. Comput. Chem.*, 2011, **32**(7), 1456–1465.

36 J. Vande Vondele and J. Hutter, Gaussian Basis Sets for Accurate Calculations on Molecular Systems in Gas and Condensed Phases, *J. Chem. Phys.*, 2007, **127**(11), 114105.

37 S. Goedecker, M. Teter and J. Hutter, Separable Dual-Space Gaussian Pseudopotentials, *Phys. Rev. B: Condens. Matter Mater. Phys.*, 1996, **54**, 1703–1710.

38 D. Dubbeldam, S. Calero, D. E. Ellis and R. Q. Snurr, RASPA: Molecular Simulation Software for Adsorption and Diffusion in Flexible Nanoporous Materials, *Mol. Simul.*, 2016, **42**(2), 81–101.

39 J. J. Potoff and J. I. Siepmann, Vapor–Liquid Equilibria of Mixtures Containing Alkanes, Carbon Dioxide, and Nitrogen, *AIChE J.*, 2004, **47**(7), 1676–1682.

40 T. Verstraelen, S. Vandenbrande, F. Heidar-Zadeh, L. Vanduyfhuys, V. Van Speybroeck, M. Waroquier and P. W. Ayers, Minimal Basis Iterative Stockholder: Atoms in Molecules for Force-Field Development, *J. Chem. Theory Comput.*, 2016, **12**, 3894–3912, DOI: 10.1021/acs.jctc.6b00456.

41 S. L. Mayo, B. D. Olafson and W. A. Goddard, DREIDING: A Generic Force Field for Molecular Simulations, *J. Phys. Chem.*, 1990, **94**(26), 8897–8909.

42 S. Vandenbrande, T. Verstraelen, J. J. Gutiérrez-Sevillano, M. Waroquier and V. Van. Van Speybroeck, Methane Adsorption in Zr-Based MOFs: Comparison and Critical Evaluation of Force Fields, *J. Phys. Chem. C*, 2017, **121**(45), 25309–25322, DOI: 10.1021/acs.jpcc.7b08971.

43 A. K. Rappe, C. J. Casewit, K. S. Colwell, W. A. Goddard III and W. M. Skiff, UFF, a Full Periodic Table Force Field for Molecular Mechanics and Molecular Dynamics Simulations, *J. Am. Chem. Soc.*, 1992, **114**(25), 10024–10035.

44 A. L. Khan, S. Basu, A. Cano-odena and I. F. J. Vankelecom, Novel High Throughput Equipment for Membrane-Based Gas Separations, *J. Membr. Sci.*, 2010, **354**(1–2), 32–39, DOI: 10.1016/j.memsci.2010.02.069.

45 J. Didden, R. Thür, A. Volodin and I. F. J. Vankelecom, Blending PPO-Based Molecules with Pebax MH 1657 in Membranes for Gas Separation, *J. Appl. Polym. Sci.*, 2018, **135**, 46433, DOI: 10.1002/app.46433.

46 R. Thür, V. Lemmens, D. Van Havere, M. van Essen, K. Nijmeijer and I. F. J. Vankelecom, Tuning 6FDA-DABA Membrane Performance for CO_2 Removal by Physical Densification and Decarboxylation Cross-Linking during Simple Thermal Treatment, *J. Membr. Sci.*, 2020, **610**, 118195, DOI: 10.1016/j.memsci.2020.118195.

47 J. Hafizovic, M. Bjørgen, U. Olsbye, P. D. C. Dietzel, S. Bordiga, C. Prestipino, C. Lamberti and K. P. Lillerud, The Inconsistency in Adsorption Properties and Powder XRD Data of MOF-5 Is Rationalized by Framework Interpenetration and the Presence of Organic and Inorganic Species in the Nanocavities, *J. Am. Chem. Soc.*, 2007, (No. 7), 3612–3620, DOI: 10.1021/ja0675447.

48 S. Øien-ØDegaard, G. C. Shearer, D. S. Wragg and K. P. Lillerud, Pitfalls in Metal–Organic Framework Crystallography: Towards More Accurate, *Chem. Soc. Rev.*, 2017, **46**, 4867–4876, DOI: 10.1039/c6cs00533k.

49 B. Chen, X. Wang, Q. Zhang, X. Xi, J. Cai, H. Qi, S. Shi, J. Wang, D. Yuan and M. Fang, Synthesis and Characterization of the Interpenetrated MOF-5, *J. Mater. Chem.*, 2010, **20**, 3758–3767, DOI: 10.1039/b922528e.

50 K. Xuan, Y. Pu, F. Li, J. Luo, N. Zhao and F. Xiao, Metal–Organic Frameworks MOF-808-X as Highly Efficient Catalysts for Direct Synthesis of Dimethyl Carbonate from CO2 and Methanol, *Chin. J. Catal.*, 2019, **40**, 533–566, DOI: 10.1016/S1872-2067(19)63291-2.

51 Y. Jiang, C. Liu, J. Caro and A. Huang, A New UiO-66-NH2 Based Mixed-Matrix Membranes with High CO_2/CH_4 Separation Performance, *Microporous Mesoporous Mater.*, 2019, **274**(July 2018), 203–211, DOI: 10.1016/j.micromeso.2018.08.003.

52 B. C. Smith, *Infrared Spectral Interpretation: A Systematic Approach*, CRC Press LLC, 1998.

53 S. Kumar, A. K. Rai, S. B. Rai and D. K. Rai, Infrared and Raman Spectra of Histidine: An Ab Initio DFT Calculations of Histidine Molecule and Its Different Protonated Forms, *Indian J. Phys.*, 2010, **84**, 563–573, DOI: 10.1007/s12648-010-0039-6.

54 S. G. Stepanian, I. D. Reva, E. D. Radchenko and G. G. Sheina, Infrared Spectra of Benzoic Acid Monomers and Dimers in Argon Matrix, *Vib. Spectrosc.*, 1996, **11**, 123–133, DOI: 10.1016/0924-2031(95)00068-2.

55 J. Jiang, F. Gándara, Y.-B. Zhang, K. Na, O. M. Yaghi and W. G. Klemperer, Superacidity in Sulfated Metal-Organic Framework-808, *J. Am. Chem. Soc.*, 2014, **136**, 12844–12847, DOI: 10.1021/ja507119n.

56 R. Williams, W. P. Jencks and F. H. Westheimer, *pK_a Data Compiled by R. Williams*, 2011, https://www.chem.wisc.edu/areas/reich/pkatable/pKa_compilation-1-Williams.pdf, accessed Mar 19, 2020.

57 G. Fan, Y. Liu and H. Wang, Identification of Thermophilic Proteins by Incorporating Evolutionary and Acid Dissociation Information into Chou's General Pseudo Amino Acid Composition, *J. Theor. Biol.*, 2016, **407**, 138–142, DOI: 10.1016/j.jtbi.2016.07.010.

58 J. Xu, J. Liu, X. Wang, Y. Xu, S. Chen and X. Wang, Optimized Synthesis of Zr(IV) Metal Organic Frameworks (MOFs-808) for Efficient Hydrogen Storage, *New J. Chem.*, 2019, **43**(2), 4092–4099, DOI: 10.1039/c8nj06362a.

59 S. Wendy and L. Queen, An Experimental and Computational Study of CO2 Adsorption in the Sodalite-Type M-BTT (M^1_4Cr,Mn,Fe,Cu) Metal–Organic Frameworks Featuring Open Metal Sites, *Chem. Sci.*, 2018, **9**, 4579, DOI: 10.1039/c8sc00971f.

60 D.-X. Xue, A. J. Cairns, Y. Belmabkhout, L. Wojtas, Y. Liu, M. H. Alkordi and M. Eddaoudi, Tunable Rare-Earth Fcu-MOFs: A Platform for Systematic Enhancement of CO_2 Adsorption Energetics and Uptake, *J. Am. Chem. Soc.*, 2013, **135**, 7660–7667, DOI: 10.1021/ja401429x.

61 H.-Y. Cho, D.-A. Yang, J. Kim, S.-Y. Jeong and W.-S. Ahn, CO_2 Adsorption and Catalytic Application of Co-MOF-74 Synthesized by Microwave Heating, *Catal. Today*, 2012, **185**(1), 35–40, DOI: 10.1016/j.cattod.2011.08.019.

62 B. Arstad, H. Fjellvåg, K. O. Kongshaug, O. Swang and R. Blom, Amine Functionalised Metal Organic Frameworks (MOFs) as Adsorbents for Carbon Dioxide, *Adsorption*, 2008, **14**, 755–762, DOI: 10.1007/s10450-008-9137-6.

63 J. A. Mason, K. Sumida, Z. R. Herm, R. Krishna and J. R. Long, Evaluating Metal–Organic Frameworks for Post-Combustion Carbon Dioxide Capture via Temperature Swing Adsorption, *Energy Environ. Sci.*, 2011, **4**, 3030–3040, DOI: 10.1039/c1ee01720a.

64 M. I. Hossain, J. D. Cunningham, T. M. Becker, B. E. Grabicka, K. S. Walton, B. D. Rabideau and T. G. Glover, Impact of MOF Defects on the Binary Adsorption of CO2 and Water in UiO-66, *Chem. Eng. Sci.*, 2019, **203**, 146–357, DOI: 10.1016/j.ces.2019.03.053.

65 A. Koutsianos, E. Kazimierska, A. R. Barron, M. Taddei and E. Andreoli, A New Approach to Enhancing the CO_2 Capture Performance of Defective UiO-66 *via* Post-Synthetic Defect Exchange, *Dalton Trans.*, 2019, **48**, 3349–3359, DOI: 10.1039/c9dt00154a.

66 P. Deria, J. E. Mondloch, E. Tylianakis, P. Ghosh, W. Bury, R. Q. Snurr, J. T. Hupp and O. K. Farha, Perfluoroalkane Functionalization of NU-1000 via Solvent-Assisted Ligand Incorporation: Synthesis and CO_2 Adsorption Studies, *J. Am. Chem. Soc.*, 2013, **14**, 16801–16804, DOI: 10.1021/ja408959g.

67 A. M. Plonka, T. G. Grissom, D. G. Musaev, A. Balboa, W. O. Gordon, D. L. Collins-Wildman, S. K. Ghose, Y. Tian, A. M. Ebrahim, M. B. Mitchell, *et al.*, Effect of Carbon Dioxide on the Degradation of Chemical Warfare Agent Simulant in the Presence of Zr Metal Organic Framework MOF-808, *Chem. Mater.*, 2019, **31**, 9904–9914, DOI: 10.1021/acs.chemmater.9b04565.

68 L. Luconi, G. Mercuri, T. Islamoglu, A. Fermi, G. Bergamini, G. Giambastiani and A. Rossin, Benzothiazolium-Functionalized NU-1000: A Versatile Material for Carbon Dioxide Adsorption and Cyanide Luminescence Sensing, *J. Mater. Chem. C*, 2020, **8**, 7492–7500, DOI: 10.1039/d0tc01436b.

69 T. G. Grissom, D. M. Driscoll, D. Troya, N. S. Sapienza, P. M. Usov, A. J. Morris and J. R. Morris, Molecular-Level Insight into CO_2 Adsorption on the Zirconium-Based Metal–Organic Framework, UiO-66: A Combined Spectroscopic and Computational Approach, *J. Phys. Chem. C*, 2019, **123**, 13731–13738, DOI: 10.1021/acs.jpcc.9b02513.

70 C. H. Lau, R. Babarao and M. R. Hill, A Route to Drastic Increase of CO_2 Uptake in Zr Metal Organic Framework UiO-66, *Chem. Commun.*, 2013, **49**(207890), 3634–3637, DOI: 10.1039/c3cc40470f.

71 T. S. Chung, L. Y. Jiang, Y. Li and S. Kulprathipanja, Mixed Matrix Membranes (MMMs) Comprising Organic Polymers with Dispersed Inorganic Fillers for Gas Separation, *Prog. Polym. Sci.*, 2007, **32**(4), 483–507, DOI: 10.1016/j.progpolymsci.2007.01.008.

72 J. Ahn, W. J. Chung, I. Pinnau, J. Song, N. Du, G. P. Robertson and M. D. Guiver, Gas Transport Behavior of Mixed-Matrix Membranes Composed of Silica Nanoparticles in

a Polymer of Intrinsic Microporosity (PIM-1), *J. Membr. Sci.*, 2010, **346**(2), 280–287, DOI: 10.1016/j.memsci.2009.09.047.

73 C. Ma and J. J. Urban, Enhanced CO_2 Capture and Hydrogen Purification by Hydroxy Metal–Organic Framework/Polyimide Mixed Matrix Membranes, *ChemSusChem*, 2019, **12**, 1–8, DOI: 10.1002/cssc.201902248.

74 J. G. H. Wijmans and R. W. Baker, *The Solution-Diffusion Model: A Unified Approach to Membrane Permeation*, 2006. DOI: 10.1002/047002903X.ch5.

75 S. Matteucci, Y. Yampolskii, B. D. Freeman and I. Pinnau, Transport of Gases and Vapors in Glassy and Rubbery Polymers, in *Materials Science of Membranes for Gas and Vapor Separation*, 2006, pp. 1–48.

76 T. Dingel, M. Tessema, S. R. Venna, G. Dahe, D. P. Hopkinson, H. M. El-kaderi and A. K. Sekizkardes, Incorporation of Benzimidazole Linked Polymers into Matrimid to Yield Mixed Matrix Membranes with Enhanced CO_2/N_2 Selectivity, *J. Membr. Sci.*, 2018, **554**(January), 90–96, DOI: 10.1016/j.memsci.2018.02.054.

77 M. Shan, B. Seoane, A. Pustovarenko, X. Wang and X. Liu, Benzimidazole Linked Polymers (BILPs) in Mixed-Matrix Membranes: Influence of Filler Porosity on the CO_2/N_2 Separation Performance, *J. Membr. Sci.*, 2018, **566**(May), 213–222, DOI: 10.1016/j.memsci.2018.08.023.

78 S. R. Venna, M. Lartey, T. Li, A. Spore, S. Kumar, H. B. Nulwala, D. R. Luebke, L. Rosi and E. Albenze, Fabrication of MMMs with Improved Gas Separation Properties Using Externally-Functionalized MOF Particles, *J. Mater. Chem. A*, 2015, **3**, 5014–5022, DOI: 10.1039/C4TA05225K.

79 S. Ross, *Introduction to Probability and Statistics for Engineers and Scientists*, 4th edn, 2009.

80 M. Vinoba, M. Bhagiyalakshmi, Y. Alqaheem, A. A. Alomair, A. Pérez and M. S. Rana, Recent Progress of Fillers in Mixed Matrix Membranes for CO_2 Separation: A Review, *Sep. Purif. Technol.*, 2017, **188**, 431–450, DOI: 10.1016/j.seppur.2017.07.051.

81 D. R. Paul and W. J. Koros, Effect of Partially Immobilizing Sorption on Permeability and the Diffusion Time Lag, *J. Polym. Sci.*, 1976, **14**, 675–685.

